Low-temperature laser-stimulated controllable generation of micro-bubbles in a water suspension of absorptive colloid particles

Angelsky, O. V.; Bekshaev, A. Ya; Maksimyak, P. P.; Maksimyak, A. P.; Hanson, Steen Grüner

Published in:
Optics Express

Link to article, DOI:
10.1364/OE.26.013995

Publication date:
2018

Document Version
Publisher's PDF, also known as Version of record

Research Article | Vol. 26, No. 11 | 28 May 2018 | OPTICS EXPRESS 13995
Optics EXPRESS

Low-temperature laser-stimulated controllable generation of micro-bubbles in a water suspension of absorptive colloid particles

O. V. ANGELSKY,[1,*] A. YA. BEKSHAEV,[2] P. P. MAKSIMYAK,[1] A. P. MAKSIMYAK,[1] AND S. G. HANSON[3]

[1]*Correlation Optics Department, Chernivtsi National University, 2, Kotsyubinsky Str., Chernivtsi 58012,Ukraine*
[2] *Physics Research Institute, I.I. Mechnikov National University, Dvorianska 2, Odessa 65082, Ukraine*
[3]*DTU Fotonik, Department of Photonics Engineering, DK-4000 Roskilde, Denmark*
**angelsky@itf.cv.ua*

Abstract: A method is described for the generation of micrometer-sized vapor-gas bubbles in a water suspension containing absorptive pigment nanoparticles. The diluted suspension (mean interparticle distance 20 μm) absorbs the continuous laser radiation (wavelength 808 nm), and each particle in the best illuminated volume (~10 × 10 × 200 μm^3) serves as a bubble-nucleation center. The suspension heating is inessential (several degrees above the room temperature) and the bubbles are formed mainly of the air gases dissolved in water. The bubbles can stably exist within or near the illuminated area where their location is governed by the competition between thermal and optical forces and can be controlled via the laser beam parameters. The method enables controllable creation, support, prescribed transportation, and destruction of the bubbles. This can be useful in applications aimed at precise sorting, transportation, and delivery of species in nano- and micro-engineering as well as for biomedical studies.

OCIS codes: (140.3390) Laser materials processing; (260.2110) Electromagnetic optics; (260.2160) Energy transfer; (350.4855) Optical tweezers or optical manipulation; (350.4990) Particles.

References and links

1. G. Baffou and H. Rigneault, "Femtosecond-Pulsed Optical Heating of Gold Nanoparticles," Phys. Rev. B **84**(3), 035415 (2011).
2. Z. Fang, Y. R. Zhen, O. Neumann, A. Polman, F. J. García de Abajo, P. Nordlander, and N. J. Halas, "Evolution of light-induced vapor generation at a liquid-immersed metallic nanoparticle," Nano Lett. **13**(4), 1736–1742 (2013).
3. D. A. Boyd, J. R. Adleman, D. G. Goodwin, and D. Psaltis, "Chemical separations by bubble-assisted interphase mass-transfer," Anal. Chem. **80**(7), 2452–2456 (2008).
4. D. A. Boyd, L. Greengard, M. Brongersma, M. Y. El-Naggar, and D. G. Goodwin, "Plasmon-assisted chemical vapor deposition," Nano Lett. **6**(11), 2592–2597 (2006).
5. C. Li, Z. Wang, P. I. Wang, Y. Peles, N. Koratkar, and G. P. Peterson, "Nanostructured copper interfaces for enhanced boiling," Small **4**(8), 1084–1088 (2008).
6. E. Lukianova-Hleb, Y. Hu, L. Latterini, L. Tarpani, S. Lee, R. A. Drezek, J. H. Hafner, and D. O. Lapotko, "Plasmonic nanobubbles as transient vapor nanobubbles generated around plasmonic nanoparticles," ACS Nano **4**(4), 2109–2123 (2010).
7. J. Kao, X. Wang, J. Warren, J. Xu, and D. Attinger, "A bubble-powered micro-rotor: conception, manufacturing, assembly and characterization," J. Micromech. Microeng. **17**(12), 2454–2460 (2007).
8. A. Hashmi, G. Yu, M. Reilly-Collette, G. Heiman, and J. Xu, "Oscillating bubbles: a versatile tool for lab on a chip applications," Lab Chip **12**(21), 4216–4227 (2012).
9. C. Zhao, Y. Liu, Y. Zhao, N. Fang, and T. J. Huang, "A reconfigurable plasmofluidic lens," Nat. Commun. **4**, 2305 (2013).
10. P. Marmottant and S. Hilgenfeldt, "A bubble-driven microfluidic transport element for bioengineering," Proc. Natl. Acad. Sci. U.S.A. **101**(26), 9523–9527 (2004).
11. S. Lal, S. E. Clare, and N. J. Halas, "Nanoshell-enabled photothermal cancer therapy: Impending clinical impact," Acc. Chem. Res. **41**(12), 1842–1851 (2008).

#327839 https://doi.org/10.1364/OE.26.013995
Journal © 2018 Received 6 Apr 2018; revised 1 May 2018; accepted 7 May 2018; published 16 May 2018

Optics EXPRESS

12. M. Delcea, N. Sternberg, A. M. Yashchenok, R. Georgieva, H. Bäumler, H. Möhwald, and A. G. Skirtach, "Nanoplasmonics for dual-molecule release through nanopores in the membrane of red blood cells," ACS Nano **6**(5), 4169–4180 (2012).
13. P. Ghosh, G. Han, M. De, C. K. Kim, and V. M. Rotello, "Gold nanoparticles in delivery applications," Adv. Drug Deliv. Rev. **60**(11), 1307–1315 (2008).
14. G. Baffou, J. Polleux, H. Rigneault, and S. Monneret, "Super-heating and micro-bubble generation around plasmonic nanoparticles under cw illumination," J. Phys. Chem. C **118**(9), 4890–4898 (2014).
15. O. V. Angelsky, A. Ya. Bekshaev, P. P. Maksimyak, A. P. Maksimyak, S. G. Hanson, and S. M. Kontush, "Controllable generation and manipulation of micro-bubbles in water with absorptive colloid particles by CW laser radiation," Opt. Express **25**(5), 5232–5243 (2017).
16. Y. Y. Geguzin, *Bubbles* (Moscow, Nauka, 1985) (In Russian).
17. A. Miniewicz, S. Bartkiewicz, H. Orlikowska, and K. Dradrach, "Marangoni effect visualized in two-dimensions optical tweezers for gas bubbles," Sci. Rep. **6**(1), 34787 (2016).
18. N. A. Ivanova and B. A. Bezuglyi, "Optical thermocapillary bubble trap," Tech. Phys. Lett. **32**(10), 854–856 (2006).
19. J. G. Ortega-Mendoza, J. A. Sarabia-Alonso, P. Zaca-Morán, A. Padilla-Vivanco, C. Toxqui-Quitl, I. Rivas-Cambero, J. Ramirez-Ramirez, S. A. Torres-Hurtado, and R. Ramos-García, "Marangoni force-driven manipulation of photothermally-induced microbubbles," Opt. Express **26**(6), 6653–6662 (2018).
20. O. V. Angelsky, A. Ya. Bekshaev, P. P. Maksimyak, A. P. Maksimyak, S. G. Hanson, and C. Yu. Zenkova, "Self-action of continuous laser radiation and Pearcey diffraction in a water suspension with light-absorbing particles," Opt. Express **22**(3), 2267–2277 (2014).
21. C. Mowry and J. R. Leger, "Large-area, single-transverse-mode semiconductor laser with diffraction-limited super-Gaussian output," Appl. Phys. Lett. **66**(13), 1614–1616 (1995).
22. C. Mätzler, MATLAB functions for Mie scattering and absorption, Version 2, IAP Research Report, No. 2002–11 (Institut für angewandte Physik, Universität Bern, 2002).
23. K. F. Palmer and D. Williams, "Optical properties of water in the near infrared," J. Opt. Soc. Am. **64**(8), 1107–1110 (1974).
24. N. V. Tsederberg, *Thermal conductivity of gases and liquids* (Massachusetts Institute of Technology, 1965).
25. J. C. Ramirez-San-Juan, E. Rodriguez-Aboytes, A. E. Martinez-Canton, O. Baldovino-Pantaleon, A. Robledo-Martinez, N. Korneev, and R. Ramos-Garcia, "Time-resolved analysis of cavitation induced by CW lasers in absorbing liquids," Opt. Express **18**(9), 8735–8742 (2010).
26. J. P. Padilla-Martinez, C. Berrospe-Rodriguez, G. Aguilar, J. C. Ramirez-San-Juan, and R. Ramos-Garcia, "Optic cavitation with CW lasers: A review," Phys. Fluids **26**(12), 122007 (2014).
27. N. B. Vargaftik, B. N. Volkov, and L. D. Voljak, "International tables of the surface tension of water," J. Phys. Chem. Ref. Data **12**(3), 817–820 (1983).
28. The Engineering ToolBox, https://www.engineeringtoolbox.com/air-properties-viscosity-conductivity-heat-capacity-d_1509.html
29. The Engineering ToolBox, https://www.engineeringtoolbox.com/overall-heat-transfer-coefficient-d_434.html
30. C. Yang, C. Yang, T. Dabros, D. Li, J. Czarnecki, and J. H. Masliyah, "Measurement of the zeta potential of gas bubbles in aqueous solutions by microelectrophoresis method," J. Colloid Interface Sci. **243**(1), 128–135 (2001).
31. W. Jia, S. Ren, and B. Hu, "Effect of water chemistry on zeta potential of air bubbles," Electrochem. Sci. **8**, 5828–5837 (2013).
32. A. Ashkin, J. M. Dziedzic, J. E. Bjorkholm, and S. Chu, "Observation of a single-beam gradient force optical trap for dielectric particles," Opt. Lett. **11**(5), 288–290 (1986).
33. A. Y. Bekshaev, "Subwavelength particles in an inhomogeneous light field: optical forces associated with the spin and orbital energy flows," J. Opt. **15**(4), 044004 (2013).
34. L. D. Landau and E. M. Lifshitz, *Fluid Mechanics* (Oxford, Pergamon Press, 1987).

1. Introduction

During the past years, great attention has been attracted to the generation and manipulation of nano- and microbubbles in aqueous solutions [1–14]. Such bubbles are proven to be suitable instruments in many fundamental and technical studies relating the micro- and nanoscale processes: investigations of water superheating and phase transitions [1–6], design of microhydraulic devices for mechanical manipulation [7,8], microoptics [9], biomedical applications including precise sorting, delivery and treatment of nano-objects [11–13].

For the majority of applications, the well-concentrated laser radiation supplies the most convenient means for the bubble formation and manipulation. In this view, the possibility of a sharply localized water heating near absorptive nanoparticles deserves a special interest [2,14,15]. Under conditions of a CW laser radiation, near-stationary regimes of bubble evolution permitting their detailed investigation and control are enabled. From a practical point of view, the near-stationary long-living bubbles are especially helpful for the precise

Optics EXPRESS

mass transfer, highly selective chemical actions, targeted transport of biological cells and species, etc [3,4,6,8–13].

Recently, we reported a simple method for generation and manipulation of microbubbles in water suspension containing colloidal light-absorbing nanoparticles [15]. The suspension was formed by diluted black ink for jet printers and was heated by a moderately focused beam from a near-IR CW laser. As described in [15], the bubbles were formed around the ink particles due to the superheated water evaporation. Additionally, due to the relatively high absorption coefficient $\alpha = 0.6$ cm^{-1} and to the great number of closely spaced heating centers, the water within the illuminated volume was also heated to rather high temperature. The bubbles thus consisted predominately of vapor and were surrounded by the high-temperature environment created by the laser beam. This enabled efficient regulation of the bubbles' generation, evolution and motion by means of the easily controllable properties of the laser radiation. The bubbles formed ensembles and quasi-ordered structures and were kept together within the most heated area of water, which was explained based on the effective thermocapillary force owing to the temperature-induced surface tension inhomogeneity (Marangoni force [16–19]). However, the repulsive interaction between the bubbles was associated with the double electric layers at the bubble–water interfaces that are hardly controllable. In that situation, the only channel for spatial manipulation of the bubbles was thermal, that is, rather inertial and inconvenient for a lot of applications (in particular, the bio-medical ones) where high-temperature regimes are not desirable.

In the present work, we describe another possibility for laser-induced controllable generation of microbubbles in water. Contrary to [15], the suspension was additionally diluted so that superheating of the nearest vicinity of a single pigment particle provided but a weak warming of the ambient water volume. In such conditions, microbubbles can still be generated around the absorbing pigment particles but they predominantly contain the air gases dissolved in water [14]. Their existence and evolution are governed by a sensitive balance between the energy supplied due to the particle's absorption and the heat and mass diffusivity in the ambient water, which also offers relevant channels for controlling the bubbles. Additionally, because of a weak water heating and tighter laser beam focusing, the thermocapillary force becomes comparable with the optical forces caused by the laser beam inhomogeneity. Their competition provides some interesting and potentially useful manifestations in the bubbles' motion and spatial localization that can be employed in practice.

2. Experiment

2.1. Experimental equipment

The scheme of the experimental setup is presented in Fig. 1(a). Like in [15], we used the water suspension of the black pigment ink (InkTec Corporation [20]) in the cylindrical glass cuvette 3 with inner diameter $D = 10$ mm and height 2 mm; the cuvette bottom being formed by a glass plate, the upper liquid surface being free. The suspension is heated by the radiation of the semiconductor laser 1 (Wavespectrum, WSLD-808-003-C, wavelength in vacuum $\lambda =$ 808 nm). Contrary to [15], the short-focus objective 2 was employed with focusing within a cone angle 20° due to which the focal spot size was essentially reduced both in the transverse and longitudinal direction, as is shown in Fig. 1(b). In fact, the objective performed a projection of the irradiating *p-n* junction onto the image plane that was chosen to coincide with the water free (upper) surface. As a result, the intensity distribution within the focal spot was close to the super-Gaussian [21] and could be approximated as

$$I(x,y) = \frac{Q_0}{\xi b_x b_y} \exp\left[-\left(\frac{x}{b_x}\right)^4 - \left(\frac{y}{b_y}\right)^4 \right], \qquad (1)$$

Optics EXPRESS

where Q_0 is the total beam power, b_x and b_y are the beam size parameters and

$$\xi = 3.286. \tag{2}$$

is the normalization coefficient. In our experiments, b_y varied from 1.5 to 7 μm with the average $b_y \approx 4$ μm, $b_x \approx 1.5\, b_y$ (see Figs. 4–7 below).

In such conditions, with account for the water refractive index

$$n_w = 1.33, \tag{3}$$

the focal depth can be estimated as the Rayleigh length of a Gaussian beam with the similar focal spot geometry,

$$n_w \left(2\pi / \lambda\right) b_y^2 \sim 0.3\ \text{mm}. \tag{4}$$

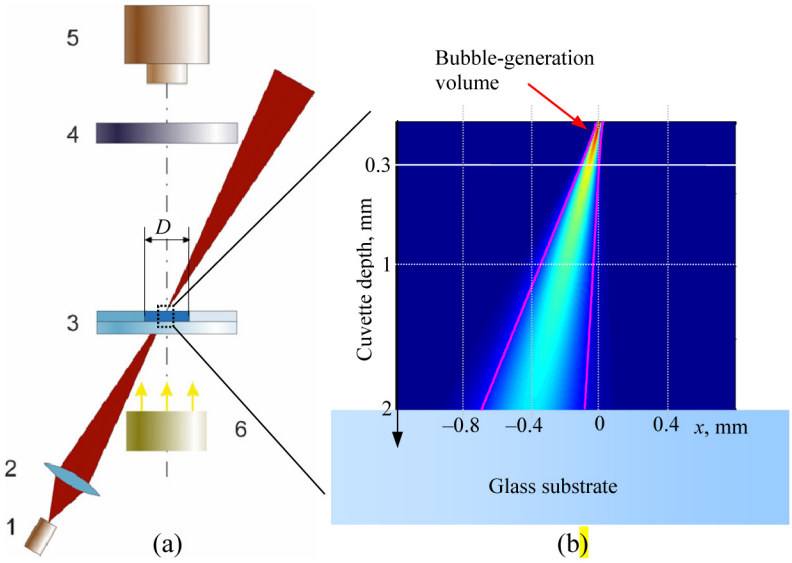

Fig. 1. (a) The experimental setup: (1) IR laser, (2) objective, (3) cuvette with the water suspension of absorbing nanoparticles, (4) spectral filter to stop the IR radiation, (5) CCD camera, (6) white-light source for visible illumination. (b) Magnified image of the central part of the cuvette (dotted rectangle in (a)) with a schematic of the focused beam: the magenta lines show the beam margins with the e^{-1} intensity level, the coordinate origin coincides with the geometric focal point.

This means that the highest energy concentration took place in the sub-surface layer marked by the white solid line in Fig. 1(b). Near the cuvette bottom (at the beam "entrance") the spot size amounts approximately $b_{x,y} \approx 300$ μm (see Fig. 1(b)) so the conditions for bubble generation within the most of the cuvette volume are not favorable. The bubbles are only formed in the limited near-surface region not deeper than the focal depth (4) and enclosed by the focused beam envelope; this region is shown in Fig. 1(b) between the magenta lines and the horizontal white line indicating 0.3 mm depth. However, the absorbed energy in the cuvette depth is the same as near the surface and the contribution of the depth to the total water heating is approximately equal for all horizontal layers.

To visualize the bubble generation and evolution, the near-spot region of the cuvette was illuminated by the white-light source 6, and its image was registered by the 1.3-megapixel CCD camera 5 protected from the direct IR radiation by the IR-protective cover glass 4. However, in case of normal incidence of the IR laser beam, the IR power reaching the CCD camera was too high even in the presence of the IR filter; to additionally protect the CCD

Optics EXPRESS

camera from the laser radiation, the heating IR beam was directed to the cuvette obliquely (see Fig. 1), approximately at an angle of 15°. This caused a slight asymmetry of the cuvette heating and resulted in parasitic convective flows which, however, almost did not affect the bubble behavior and thus additionally testified for their stable and controllable nature. The receiving optical system 5 was designed to image the near-surface layer of the cuvette suspension. The IR laser power was adjustable within the range 0.1 W to 1.5 W.

2.2. Suspension properties

The water suspension contains pigment colloidal particles consisting of a spherical polymer core with mean radius a_c = 80 nm covered with a resin shell of thickness a_s = 20 nm, so the mean particle radius is $a = a_c + a_s$ = 100 nm with the geometric cross section

$$\sigma = \pi a_p{}^2 = 3.14\times10^{-10}\,\mathrm{cm}^2. \tag{5}$$

The core and shell refraction indices amount to n_c = 1.59 and n_s = 1.58 + 0.74i, respectively. For these data, the extinction σ_{ext} and absorption σ_{abs} cross sections can be calculated using the Mie theory [22]. The results are suitably expressed via the corresponding efficiencies

$$\bar{\sigma}_{\mathrm{ext}} = \frac{\sigma_{\mathrm{ext}}}{\sigma}, \quad \bar{\sigma}_{\mathrm{abs}} = \frac{\sigma_{\mathrm{abs}}}{\sigma} \tag{6}$$

where

(i) if the ambient medium is water,

$$\bar{\sigma}_{\mathrm{ext}} = \bar{\sigma}_{\mathrm{ext},w} = 0.587, \quad \bar{\sigma}_{\mathrm{abs}} = \bar{\sigma}_{\mathrm{abs},w} = 0.543; \tag{7}$$

(ii) if the ambient medium is vapor (air), and instead of Eq. (3) n = 1,

$$\bar{\sigma}_{\mathrm{ext}} = 0.539, \quad \bar{\sigma}_{\mathrm{abs}} = 0.471. \tag{8}$$

The values (8) are applicable when, due to the particle heating, the vapor layer is formed between the particle and the liquid water [14].

In contrast to the previous work [15], for the new experiments, the ink suspension was additionally diluted so that the absorption coefficient measured via the light attenuation equals

$$a_w = 0.024\,\mathrm{cm}^{-1}. \tag{9}$$

With account for the intrinsic absorption of water at this wavelength α_0 = 0.019 cm^{-1} [23], this value enables us to estimate the particles' concentration via expression

$$N = \frac{\alpha_w - \alpha_0}{\sigma_{\mathrm{abs},w}}. \tag{10}$$

After substitution of the values (9) and (7) one obtains from Eq. (10) $N \approx 0.27\cdot10^8\,\mathrm{cm}^{-3}$, which means that the mean distance between the particles is

$$N^{-1/3} \approx 3.3\cdot10^{-3}\,\mathrm{cm} = 33\ \mu\mathrm{m} \tag{11}$$

This is a rather sparse distribution that allows us to assume that each particle heats the surrounding water independently (see Sec. 3.1 below).

2.3. Mean temperature conditions in the cuvette

Each particle efficiently absorbs the incident radiation and the absorbed energy is ultimately transmitted to the ambient water where it adds up to the energy absorbed by water and causes

Optics EXPRESS

a temperature increase. Due to the relatively high intrinsic absorption of water and because of the efficient heat exchange in the water medium between the absorbing particles, from a macroscopic point of view, we can consider the suspension as a continuous medium that absorbs the light energy in each point. However, as soon as a pigment particle absorbs the light energy, its temperature exceeds the boiling temperature of water and the particle appears in a vapor environment where the absorption efficiency decreases as is described by Eqs. (7) and (8). Accordingly, the absorption coefficient also decreases compared to Eq. (9) and equals

$$\alpha = \alpha_0 + (\alpha_w - \alpha_0)\frac{\sigma_{\text{abs}}}{\sigma_{\text{abs},w}} = 0.022\ \text{cm}^{-1}. \tag{12}$$

In the continuous-medium approximation, the temperature distribution can be calculated via the Fourier law for the thermal conductivity [24], which in the stationary conditions is described by the equation

$$\kappa_w \nabla^2 T_m + F = 0, \tag{13}$$

where

$$k_w = 0.6\,\text{K}/(\text{W}\cdot\text{m}) \tag{14}$$

is the thermal conductivity coefficient of water, subscript '*m*' indicates that we deal with the mean temperature, and *F* is a function of the coordinates describing the heat source density. When the light beam propagates through the medium, the energy absorbed per unit volume is αI, where *I* is the beam intensity (energy flow density). Obviously, with the absorption coefficient (12), the beam energy decreases rather weakly during beam propagation within the cuvette; additionally, in the first approximation we may neglect the beam conical shape and its obliquity, and assume that the cuvette is illuminated in its center and consider $I = I(x, y)$ as a function of only the transverse coordinates in the form (1). Then Eq. (13) can be solved numerically with the condition that the temperature at the cuvette wall $\rho = \sqrt{x^2 + y^2} = D/2$ is fixed and equals the ambient temperature $T_D \approx 293$ K = 20 °C. The numerical analysis confirms that the mean temperature distribution is weakly sensitive to the source function changes along the cuvette depth; also, for $\rho > 2\max(b_x, b_y)$ it is almost insensitive to the source function (1) anisotropy and depends only on ρ. The results are presented in Fig. 2 for different values of the laser power used in our experiments.

In the regular regime, the experimental setup of Fig. 1 provides no possibility for temperature measurement. The temperature was estimated in a separate experiment in which the observation unit 4, 5 of Fig. 1 was removed and a thermocouple of 1 mm diameter was placed in the cuvette outside the bright spot; in this experiment the laser power was 2.0 W (blue curve in Fig. 2). In view of the coarse spatial resolution of the temperature measurement, the blue circle position reasonably agrees with the calculated model, which supports the model results obtained for other power values (red, green and cyan curves of Fig. 2).

Optics EXPRESS

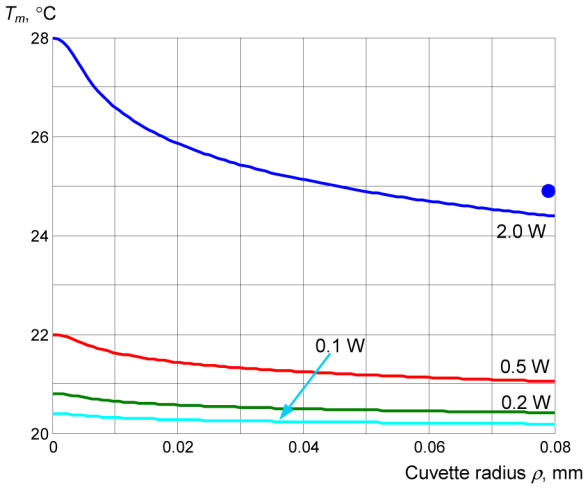

Fig. 2. Mean temperature distribution in the cuvette 3 of Fig. 1 for different values of the incident laser power Q_0 indicated near the curves. The blue circle shows the experimental result obtained for Q_0 = 2.0 W.

3. Results and discussion

3.1. Temperature conditions of the bubble generation and growth

As was reported earlier [2,14,25,26], the bubble nucleation initially occurs near a single absorbing nanoparticle in conditions of water superheating when the local temperature exceeds the standard boiling temperature 100 °C. Normally, at the moment of nucleation, the gas-vapor phase near the absorbing nanoparticle experiences a high pressure (at least, the Laplacian pressure within a bubble whose radius just slightly exceeds the particle radius 0.1 μm is $p_L = 2\gamma/a \sim 10^6$ Pa ($\gamma \approx 50\cdot10^{-3}$ N/m is the high-temperature surface tension of water [27]), which exceeds the atmospheric pressure ten times, and for which the boiling temperature reaches ~180 °C [2,14,15].

As is seen from Sec. 2.2, Eq. (11), the absorbing particles are distributed rather loosely in the water volume and the fluctuation events when two or more particles appear anomalously close to each other to cause the local "excess" of released energy [15] are unlikely. Most likely are the conditions when each particle is a center near which a bubble embryo is formed independently. After reaching the critical size, the bubble grows rapidly, and simultaneously the temperature at the bubble periphery decreases. But even when it becomes lower than the boiling point, the bubble growth continues due to diffusion of the air gases dissolved in water [14,25,26]. In a well-developed micrometer-size bubble, the temperature is normally close to the room temperature and the pressure is close to the atmospheric one. Let us consider some details of the temperature conditions accompanying this process.

The first stage of the bubble formation is the particle heating due to the absorbed light energy. For the particle radius a = 0.1 μm this process is characterized by the characteristic time scale $\tau \simeq \rho_w C_w a^2/\kappa_w \approx 7\cdot10^{-8}$ s ($\rho_w = 10^3$ kg/m^3, $C_w = 4.18\cdot10^3$ J/(kg·K) and κ_w (14) are the mass density, heat capacity and the thermal conductivity of water, respectively), which means that any transient phenomena are not observable in our experiments. Thus, the stationary model is adequate and will be used in further consideration.

The power absorbed by a single pigment particle equals $W = I\sigma_{\mathrm{abs},w}$ where $\sigma_{\mathrm{abs},w}$ is determined by Eqs. (6) and (7) because at this stage the particle is surrounded by liquid water,

Optics EXPRESS

and I is the light intensity at the particle position. For simplicity, we perform all calculations for the beam axis where $I = I_0 = Q_0 \big/ \left(\xi b_x b_y\right)$ (see Eq. (1)) and then the absorbed power is

$$W_w = \bar{\sigma}_{\mathrm{abs},w} \frac{\pi Q_0 a^2}{\xi b_x b_y}. \tag{15}$$

This power crosses a spherical surface of radius r centered at the particle's center and, according to the Fourier's law, it determines the local temperature gradient:

$$\frac{W_w}{4\pi r^2} = -\kappa_w \frac{dT}{dr} \tag{16}$$

where κ_w is given by Eq. (14). Hence, assuming spherical symmetry of the problem, the temperature distribution can be derived in the form

$$T(r) = \frac{W_w}{4\pi\kappa_w r} + T_B \tag{17}$$

with T_B being the background temperature far from the particle. We presumably identify this temperature with the mean temperature of the suspension at the particle location, calculated in Section 2.3, $T_B = T_m$. Its explicit radial dependence illustrated by Fig. 2 reflects slightly different temperature conditions for different individual particles caused by the collective light absorption of the suspension on the whole.

According to Eqs. (15) and (17), the particle temperature can be estimated as

$$T(a) = \bar{\sigma}_{\mathrm{abs},w} \frac{Q_0 a}{4\xi\kappa_w b_x b_y} + T_m \tag{18}$$

This formula, with allowance for Eqs. (2), (7) and (14) for the particle radius a = 0.1 μm, gives

$$T(a) = 6.9 \cdot 10^3 \frac{[Q_0]}{\left[b_x b_y\right]} + T_m, \tag{19}$$

where $[Q_0]$ is the beam power in Watts and $\left[b_x b_y\right]$ is the product of the beam size parameters (see Eq. (1)) measured in square micrometers. For typical experimental conditions (see Sec. 3.2)

$$b_x b_y = 24\ \mu\mathrm{m}^2 \tag{20}$$

and T_m = 24 °C the result (19) dictates that the temperature necessary for bubble nucleation (~180 °C, see the 1st paragraph of this Sec. 3.1) can be realized at the beam center if

$$Q_0 \geq 0.5 - 0.6\,\mathrm{W}, \tag{21}$$

which is close to the observed experimental threshold power for the bubbles' generation (see Sec. 3.2).

Approximately the same conditions are relevant for all the pigment particles situated within the focal depth (4); in view of the mean distance between the particles (11) this entails that, on the average, nearly 10 particles can generate the bubbles simultaneously. Just after the bubble embryo emerges, the absorbing particle appears in the new physical environment, which influences the subsequent evolution. The first consequence is that the bubble acquires Archimedean buoyancy and ascends to the free surface, so that new particles can enter the

depth of the focal region, marked by the red arrow in Fig. 1(b), because of diffusion and thus contribute to the new bubbles' formation. This qualitatively explains the formation of additional fractions of bubbles whose evolution repeats the same stages but with certain delay in time. This delay can be controlled by temporary reduction of the laser power below the generation threshold so that the existing bubbles grow while the new ones do not appear. If afterwards the power again switches above the threshold, the new group of bubbles emerge in the focal depth and travel up to the free surface to join the existing ones (see Figs. 4–7 and Visualization 1, Visualization 2, Visualization 4, and Visualization 5; note that the numbers of microbubbles in each size fraction is 7 – 15, as is dictated by the above consideration).

Now consider the thermal conditions after the bubble formation. In this situation, the absorbing particle is surrounded by the gas (vapor + air) medium with relatively low thermal conductivity [28]

$$k_g = 0.03\,\mathrm{K}/(\mathrm{W}\cdot\mathrm{m}). \tag{22}$$

Besides, the absorption efficiency in the gas environment changes and is now determined by Eq. (8) so that the absorbed power W differs from the value in water (15) and is determined by the similar expression

$$W = \frac{\bar{\sigma}_{\mathrm{abs}}}{\bar{\sigma}_{\mathrm{abs},w}} W_w = \bar{\sigma}_{\mathrm{abs}} \frac{\pi Q_0 a^2}{\xi b_x b_y} \tag{23}$$

Then, if the bubble radius is R, the temperature distribution around the particle can be presented in the form

$$T(r) = \begin{cases} \dfrac{W}{4\pi\kappa_w r} + T_m, & r > R, \\ \dfrac{W}{4\pi\kappa_g r}\left(1 - \dfrac{r}{R} + \dfrac{\kappa_g}{\kappa_w}\dfrac{r}{R}\right) + T_m, & r < R. \end{cases} \tag{24}$$

In particular, at the bubble surface

$$T(R) = \frac{W}{4\pi\kappa_w R} + T_m, \tag{25}$$

and at the absorbing particle surface

$$T(a) = \frac{W}{4\pi\kappa_g a}\left(1 - \frac{a}{R} + \frac{\kappa_g}{\kappa_w}\frac{a}{R}\right) + T_m \approx \frac{W}{4\pi\kappa_g a} + T_m. \tag{26}$$

The latter approximate equality in (26) is valid due to the usual conditions $a << R$, $\kappa_g << \kappa_w$. Upon the derivation of Eq. (24), we have neglected a possible temperature jump at the bubble-water interface. The relevance of this assumption is confirmed by the result: under conditions of Eqs. (24) – (26), for the typical heat transfer coefficient between free gas and water 5 – 15 W/m^{2}K [29] the estimated temperature jump at the water-gas interface constitutes ~0.1 K on the order of magnitude.

The temperature conditions (23) – (26) form the background for the bubble expansion after the embryo is created. Particularly, in our experimental conditions, with taking into account Eqs. (14), (22),

$$T(R) = T_m + 6.0\cdot 10^2 \frac{[Q_0]}{[b_x b_y][R]}\,\mathrm{K}, \tag{27}$$

Optics EXPRESS

$$T(a) = T_m + 1.2 \cdot 10^5 \frac{[Q_0]}{[b_x b_y]}, \tag{28}$$

where the bracketed quantities obey the same conventions as in Eq. (19), $[R]$ is the bubble radius in μm. For typical values of the spot size (20) and the beam power (21), Eq. (27) shows that at the gas–water interface the temperature falls below 100 °C as soon as the bubble radius reaches R = 0.18 μm. Further bubble growth occurs mainly due to the diffusion of gases dissolved in the ambient water; this process is discussed in detail in [14] and references therein.

One can expect that the details of the bubble evolution depend on the energy 'feeding' provided by the light absorption. Indeed, in our experiments the bubble evolution was efficiently controlled by changing the laser power Q_0. When it is switched below the above discussed bubble-generation threshold (21), new bubbles do not appear but the existing ones still grow. Contrary to [15], in the present experiments their radii never exceeded 10 μm but typically were 2 – 5 μm (see Figs. 4–7). When the power decreases to Q_0 = 0.3 W the bubble stops growing and the stationary situation occurs at which the bubbles exist for a long time with no visible change in their size. Upon smaller beam power, the bubbles visually shrink but, as a rule, rather slowly. And below Q_0 = 0.1 W they rapidly disappear (in a second or less). Some relevant estimates of the bubble evolution parameters based on Eqs. (27), (28) for the illumination beam satisfying Eq. (20) and under the typical experimental conditions are presented in Table 1.

The data of Table 1 agree with the known concept that the gas-vapor bubbles can exist without essential heating of the gas phase [14]. However, our experiments differ from the situation reported in [14] by the low concentration of absorbing particles due to which the bubbles normally do not coalesce and evolve separately. This entails that the bubbles grow slowly and normally their radii do not exceed 10 μm. Consequently, they accumulate rather small amount of gases, and their lifetime after the energy feeding stops is small. For example (see Table 1), at Q_0 = 0.1 W the temperature of the bubble is practically the same as of the ambient water, and the water temperature only weakly differs from the room temperature (Fig. 2). In such conditions, the bubble lifetime determined by approximate relation $\tau \approx 0.22R^3$ [14] for the right column of Table 1 amounts to ~1.6 s, and this practically instant shrinkage of bubbles was really observed.

Table 1. The bubble parameters and characteristic temperature values for different regimes

Parameter	Growing bubble	Stationary bubble		Bubble near collapse
Laser beam power Q_0, W	0.6	0.3		0.1
Absorbing particle temperature excess $T(a) - T_m$, K	$3 \cdot 10^3$	$1.5 \cdot 10^3$		$0.5 \cdot 10^3$
Bubble radius R, μm	2.0	2.0	4.0	2.0
Bubble surface temperature excess $T(R) - T_m$, K	7.5	3.8	1.9	1.2

3.2. Control of the bubbles' localization and motion

Similarly to what was reported in the previous publication [15], the bubbles' ensembles generated by the CW laser radiation could be observed within or very close to the IR-illuminated region (see Figs. 4–7). They are kept together by the thermocapillary force

Optics EXPRESS

emerging due to temperature inhomogeneity which induces the inhomogeneity of the surface tension γ:

$$\mathbf{F}_{\mathrm{TC}} = -\pi R^2 \frac{d\gamma}{dT} \nabla T_m . \tag{29}$$

This force appears due to the slight difference in the temperature conditions along the bubble surface [16], and its manifestations are observed and employed in many situations where the concentrated light is absorbed in organic liquids containing the absorptive particles [17–20]. In our present scheme, following Eqs. (25), (27), the temperature variations along the bubble surface can be ascribed to the ambient temperature inhomogeneity $T_m(\rho)$ discussed in Sec. 2.3, Fig. 2. In such conditions [27]

$$dg / dT = -0.17 \times 10^{-3}\,\mathrm{N/(m \cdot K)}, \tag{30}$$

the force (29) "drags" the bubbles to the most heated region. In [15] this resulted in the quasi-regular bubble distribution caused by the joint action of the "attractive" thermocapillary force and the repulsive action of the surface electric charges always present at the water–gas interfaces [30,31].

However, now the spatial distribution of the bubbles shows certain additional regularities that can be explained by the peculiar competition between the thermocapillary force (29), (30) and the optical gradient force caused by the inhomogeneous illumination [15,32,33]. In the dipole approximation this force can be estimated as

$$\mathbf{F}_{\mathrm{OG}} = \frac{2\pi n_w}{c} R^3 \frac{1-n_w^2}{1+2n_w^2} \nabla I(x,y), \tag{31}$$

where the light intensity $I(x,y)$ is determined by Eq. (1), n_w is given by Eq. (3), and c is the speed of light in vacuum. In conditions of [15] this force was also present but it was small compared to the thermocapillary force (29). In the present experiment, due to strongly reduced light absorption (12) (0.02 cm^{-1} instead of 0.6 cm^{-1} in [15]), the water heating and the corresponding temperature gradients are essentially smaller (cf. Figure 2 of this paper and Fig. 2 of [15]). Additionally, the illuminating laser beam size is reduced ($b_{x,y}$ ~5 μm instead of 50 μm in [15]), which increases the light intensity gradient, and the absolute values of both forces are now comparable.

The interplay between the thermocapillary force and the optical gradient force generated by the beam with intensity distribution (1) under the typical experimental conditions is illustrated in Fig. 3: negative force "drags" the bubble towards the spot center, positive force "pushes" it away (the positive-force region is marked by the light blue background). There are two equilibrium positions where the resulting force vanishes: stable equilibrium at point A and unstable at point B. This means that the bubbles tend to assemble at the spot periphery, which was confirmed experimentally.

One notices that there is another equilibrium point C at the spot center. Actually, the central position was seldom observed in experiments, most probably because it is not really stable, at least not for small bubbles: first, the illumination scheme destroys the spot symmetry (see Fig. 1), and, second, the thermal convective flows, inevitably existing in the inhomogeneously heated water, are most irregular in the central region and will thus carry any particle away.

Optics EXPRESS

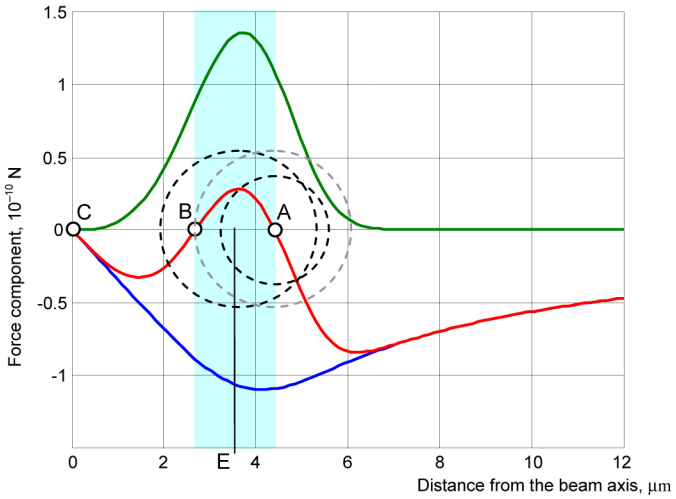

Fig. 3. Spatial dependence of the thermocapillary (29) and optical (31) y-directed forces exerted on a spherical bubble with radius 2 μm in the laser beam (1) with $Q_0 = 0.5$ W and $b_x = 6$ μm, $b_y = 4$ μm (the corresponding temperature distribution is described by the red curve of Fig. 2). Blue curve: thermocapillary force F_{TC}; green curve: optical force F_{OG}; red curve: resulting force $F_{TC} + F_{OG}$; the light blue rectangle marks the region where the resulting force is repulsive. Black circles: equilibrium points, dashed circumferences: contours of bubbles with different sizes (see further explanations in the text).

In Fig. 4 the peripheral bubbles' location is illustrated for the laser power 0.3 W and the beam size $b_x = 6$ μm, $b_y = 4$ μm (in the considered linear approximation, the thermocapillary and gradient forces are both proportional to the incident power, and its variations do not affect the interrelations between the force components). Visualization 1 shows that the peripheral location of the bubbles is rather stable, even in presence of parasitic convective flows caused by uncontrollable irregularities and the actual asymmetry of the cuvette heating due to the laser beam inclination (see Fig. 1). However, the considered forces do not prevent the bubbles' motion along directions tangential to the spot contour and really, one can see that "orbital" displacements of the bubbles frequently occur under the random action of the parasitic flows.

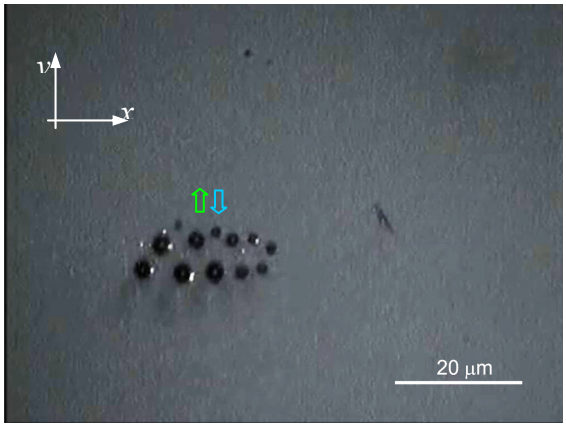

Fig. 4. (Visualization 1). A group of generated microbubbles located at the periphery of the laser beam spot. The approximate e^{-1} intensity contour of the focal spot at the water-air interface plane is shown by the cyan dotted ellipse. Green and cyan arrows show the repulsive (F_{OG}) and attractive (F_{TC}) forces that cancel each other at the current bubble's position (cf. Figure 3).

Optics EXPRESS

Moreover, strong localization of the bubbles at the beam periphery still takes place when the spot size changes. Figure 5 and Visualization 2 show modification of the bubbles' positions while the beam size is reduced from b_y = 7 μm to b_y = 3.5 μm ($b_x \approx 1.5 b_y$). Actually, by shrinking the focal spot, the bubbles can be driven so close to each other that a sort of explosive cavitation can be detected (Visualization 3). However, we did not analyze this process in detail because the stationary bubbles are the main subject of this paper.

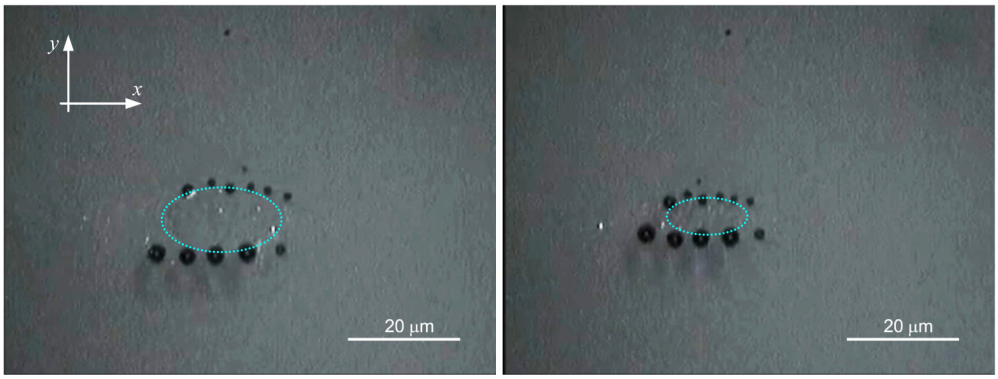

(a) (b)

Fig. 5. (Visualization 2 and Visualization 3). View of the bubble ensemble when the vertical beam size is reduced from (a) b_y = 7 μm to (b) b_y = 3.5 μm at 5th second of Visualization 2. The approximate e^{-1} intensity contours of the focal spots at the water-air interface plane are shown by the cyan dotted ellipse.

The dependences illustrated by Fig. 3 explain other regularities in the bubble location demonstrated by Fig. 6 and Visualization 4. Here the spot size is b_y = 7 μm, and the laser power Q_0 = 0.6 W provided conditions for generation of new bubbles. So the situation is realized where several fractions of bubbles are generated (see Sec. 3.1, Eq. (21) and the subsequent paragraph). When the beam power was reduced to 0.3 W, the stationary ensemble of bubbles containing different size fractions was obtained. Remarkably, the small bubbles are situated at larger distances from the beam center than the large ones. At first glance, this looks paradoxical as the ratio of the repulsive (31) and the attractive (29) forces is proportional to R and, *ceteris paribus*, the large bubbles should be repulsed stronger. However, formulas (29) and (31) used for obtaining the dependencies of Fig. 3 are approximate and assume that the temperature and intensity gradient is constant for the whole bubble. When the intensity variation within the bubble size range is more complex, the different "parts" of the bubble "feel" different influences.

This is illustrated by the dashed circles in Fig. 3 that represent the bubble "contours" superimposed onto the force graphs. Qualitatively, direction of the resulting force exerted on a bubble can be understood from comparison of the circle areas embracing "positive" and "negative" segments of the red curve (inside and outside of the light-blue area). One can see that for smaller bubbles, the resulting force is close to that calculated by the simplified formulas (29), (31), and the bubble position is close to the prescribed point of stable equilibrium A. If a larger bubble is centered at point A (dull grey dashed circle in Fig. 3), its contour is almost equally divided between the "positive" and "negative" regions but the "attractive" force (outside the light blue area) is noticeably stronger. So the bubble moves to the position marked by the black dashed contour to restore the equilibrium; its center is then situated in a certain point E which is closer the beam center than the point A.

An additional reason that smaller bubbles tend to locate more distantly from the spot center is associated with the inevitable off-center thermoconvective flows [17,34]. The corresponding drag force (Stokes force [34]) is proportional to the bubble radius R, and its relative "weight" grows while the bubble radius decreases [15].

Optics EXPRESS

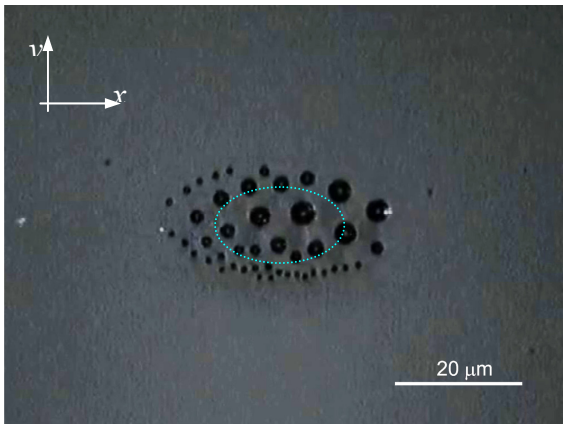

Fig. 6. (Visualization 4). Bubble ensemble with different size fractions: the large bubbles gather near the laser beam axis, the small ones keep at the beam periphery. The approximate e^{-1} intensity contour of the focal spot at the water-air interface plane is shown by the cyan dotted ellipse.

Due to this mechanism, growing bubbles sometimes completely "loose" the peripheral equilibrium position and are dragged to the beam axis. For large enough bubbles ($R \gtrsim 3.5$ μm, according to Fig. 3) this is the only possible equilibrium position; besides, the irregular perturbations in the near-center region, discussed in the description of Fig. 3, are not so important for large bubbles. This is spectacularly illustrated by Fig. 7(a,b). In this experiment the bubbles slowly grow in size, and the largest one (indicated by the white arrow) "jumps" to the spot center when its radius reaches ~4 μm (20th second of the Visualization 5). Quite probably, the same mechanism is in charge in many other situations (see, e.g., Fig. 6 and Visualization 4) but there it is masked by the presence of several bubbles situated close to each other in the central region, whose interaction [15] essentially complicates the schematized pattern of Fig. 3.

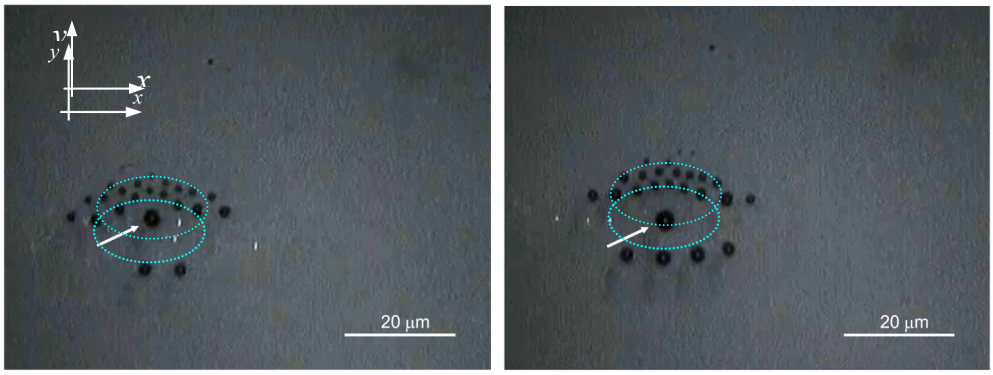

(a) (b)

Fig. 7. (Visualization 5). (a) Bubbles are located at the periphery of the light intensity distribution; the largest bubble marked by the arrow is the closest to the spot center. (b) The largest bubble grows and moves to the beam center. The approximate e^{-1} intensity contour of the focal spot at the water-air interface plane is shown by the cyan dotted ellipse.

4. Conclusion

In this paper, we describe a method for generation of micro-bubbles and their ensembles under the action of near-IR CW laser radiation. The method is based on our previous work [15] where the bubbles were formed due to local heating of the water suspension with

Optics EXPRESS

absorbing colloidal nanoparticles. In contrast to [15], the suspension is now additionally diluted so that the large mean distance between the absorbing centers excludes most of the collective heating effects; each particle acts as a heating and nucleation center independently. To make this process more efficient, we increased the light energy concentration by tighter laser beam focusing. The bubble embryos are formed due to the water evaporation but their further growth and stationary existence is regulated by the diffusion of gases dissolved in ambient water [14]. Under such conditions, the suspension heating is inessential (mean temperature of water exceeds the room temperature by several degrees), which makes the whole system less inertial and is favorable for many possible applications, especially those associated with bio-medical purposes. Moreover, by controlling the laser beam power, we can control the bubbles' emergence and growth.

An additional consequence of the new parameters of our experiment is the growing role of optical forces associated with the light beam inhomogeneity. Like in our previous experiments [15], the bubbles are kept within or near the illuminated area due to the thermocapillary force owing to the temperature-induced surface tension inhomogeneity. However, now this force is comparable with the optical gradient force that "pushes" the bubbles outside the bright spot. Most probably, their localization and motion is regulated by the competition between these two main forces, which is also favorable for the bubbles' manipulation because the optical force can be suitably regulated with high speed via the laser beam adjustment.

Like in [15], the microbubbles can be generated in a desired number (5 – 15 on the average) but their diameters, as a rule, now do not exceed 10 μm. A whole group of generated bubbles is kept within the laser-illuminated region, and we present a number of examples where the bubbles' positions, within this region, depend on their size and on the laser beam width and power. The bubbles' generation can be stopped by switching the laser power below the threshold value (0.5 – 0.6 W in our conditions) while their growth continues until the power exceeds the "growth threshold" 0.3 W. Then the stationary regime is realized when the microbubbles exist for a long period of time without visible change in sizes and numbers, and this regime is especially favorable for various manipulations with the bubbles. However, the bubbles cannot exist without certain energy "feeding" and rapidly collapse when the laser power decreases below 0.1 W.

In general, the presented method offers efficient ways by which the necessary number of bubbles can be produced, supported, transported to desirable position and collapsed at a desired moment. This can be useful for many practical applications where the microbubbles are used for precise sorting, transportation, delivery of species and targeted physico-chemical interactions in nano- and micro-engineering, including the biomedical researches.